# Enhancing Radio Frequency Performance of Graphene Field-Effect Transistors through Machine-Learning-Based Physical Prediction and Optimization

Gyeong Min Seo, Chang-Ki Baek, and Byoung Don Kong*

Read Online

ACCESS | Metrics & More | Article Recommendations

**ABSTRACT:** Graphene has excellent carrier mobility, making it highly suitable for high-speed electronics. However, controlling the carrier flow still poses significant challenges due to the lack of an energy band gap. To address this issue, researchers have explored introducing a transport gap using the pseudo-optic scheme of the massless Dirac Fermion, which has shown promising results in improving device characteristics. In this study, we demonstrate the use of a deep neural network to manage the pseudo-optic trajectories of carriers and discover an optimized geometry. The neural network operates similarly to a pinball game, where multiple intended reflections control the trajectories of steel balls. The flow of massless Dirac Fermions can be modified by well-designed reflection paths, and artificial intelligence can replace human intuition in finding an optimal design. We implement this approach using a finite-difference time-domain simulation for massless Dirac Fermions, forwarding the carriers' transmission for arbitrary gate shapes to the neural network for training. The trained neural network is then used to design an optimized gate shape for a targeted graphene field-effect transistor performance, specifically radio frequency characteristics. Using this approach, we achieved a maximum oscillation frequency ($f_{max}$) of up to 59.6 GHz for the machine-designed transistor, approximately 20 times higher than that of conventional graphene field-effect transistors with the same effective gate length.

**KEYWORDS:** graphene pseudo-optics, graphene FET, maximum oscillation frequency, deep neural network, inverse design
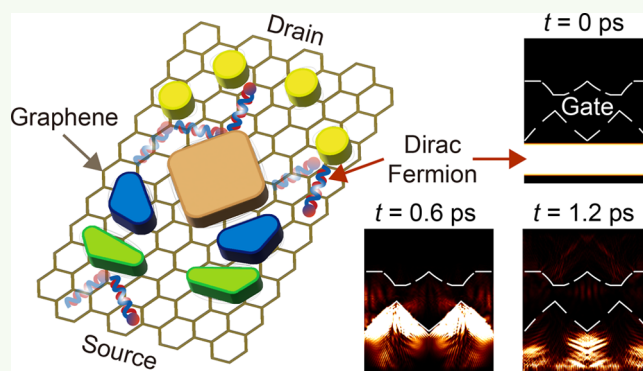
## INTRODUCTION

Graphene does not have forbidden energy levels (or energy bandgap), unlike semiconductors. This lack of energy bandgap means that carrier depletion does not occur in graphene, making it difficult to turn off a graphene field effect transistor (GFET) and limiting its application in areas requiring a high on−off ratio. However, due to its superior mobility, GFETs remain attractive in analog applications where high speed and current are more critical than the on−off ratio. The speed at which carriers can travel under the gate is crucial to the signal transfer speed of a field-effect transistor (FET). The cutoff frequency ($f_T$) of graphene, the highest frequency of signal transfer, can be very high due to its superior mobility. Assuming that electrons travel at the Fermi velocity $v_F$ ($\sim 10^6$ m·s$^{-1}$), the maximum gate length for an intrinsic cutoff frequency ($f_{T,int}$) of 0.3 THz, without any parasitic component, is about 500 nm.[1] However, the lack of carrier depletion remains an issue, resulting in no current saturation and a small output impedance ($r_{out}$). Small $r_{out}$ leads to a low maximum oscillation frequency ($f_{max}$), the highest frequency of power transfer. Consequently, while the signal can transfer fast, the power delivery in GFETs is poor. Various attempts to introduce a bandgap have been made, including nanoribbon and strain.[2−8] However, a dilemma arises as any direct alteration of the graphene lattice for a bandgap typically results in severe degradation of the mobility - the true advantage of graphene.

One potential approach to creating a transport gap without compromising mobility is to leverage the unique pseudo-optic properties of Dirac particles. By taking advantage of the negative refraction of these particles at a *p-n* junction, it is possible to redirect the flow of particles back to their starting point, creating an effective energy gap without altering the crystal structure. The angles of refraction at these junctions
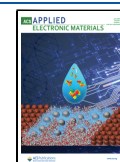
depend on the energy of the carriers, and a well-designed gate shape can significantly suppress transport for a specific energy range. For example, trapezoidal and saw-shaped gates have demonstrated improved RF performance and on−off ratios by reflecting electrons and minimizing Klein tunneling.[9,10] These gates act like oblique walls, essentially playing a game of pinball with the ballistic carriers to control their trajectories (as shown in Figure 1a). However, optimizing carrier scattering with
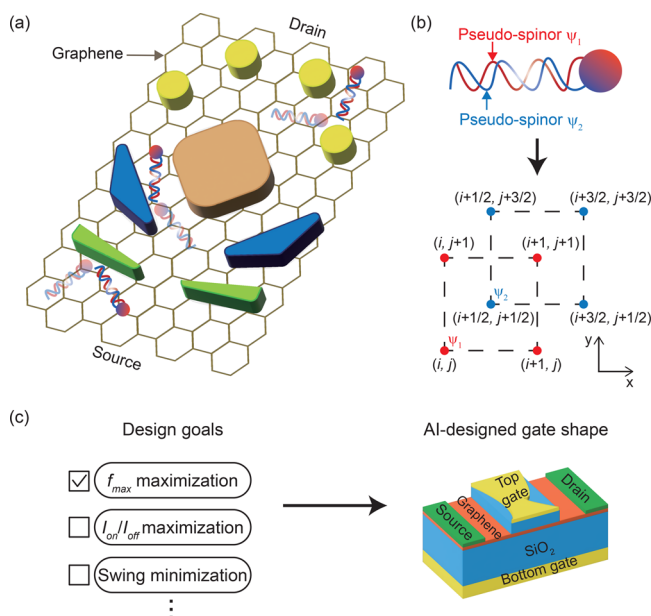


**Figure 1.** Inverse design of graphene FET by artificial intelligence. (a) Dirac particles' pinball concept. Dirac particles' trajectories are controlled by manipulating gate shape according to graphene's pseudo-optic properties. (b) Finite-difference time-domain (FDTD) method for massless Dirac Fermions (details given in the Methodology section). (c) Inverse design sequence. The AI mastering Dirac pinball game designs a gate shape to meet a design goal, particularly in structures characterized by a dual-gated architecture.

multiple refractions across arbitrary interfaces can be a complex task that is not easily accomplished by human observation alone. With a more sophisticated arrangement of these walls, it may be possible to achieve even more significant enhancements.

To overcome the limitations of human intuition in designing gate shapes for GFETs, we explore the potential of using artificial intelligence (AI) as a complement. By employing deep neural networks (DNNs) for inverse design, we aim to optimize gate shapes that maximize the RF performance of GFETs. Originally developed in computer science for tasks such as image clarification and speech recognition,[11,12] machine-learning techniques are now being applied in various physical systems to predict responses, design structures for specific purposes, and more. For example, DNNs have been shown to accurately predict quantum mechanical many-body systems,[13,14] uncover hidden photonic structures,[15−18] and design a porous graphene with specific properties, such as low

thermal conductivity.[19] In this study, we train a DNN to establish correlations between GFET gate shapes and the resulting transmission, using finite-difference time-domain (FDTD) simulations for massless Dirac Fermions. With the trained DNN, we can design gate shapes that exhibit targeted GFET characteristics, such as high $r_{out}$ and $f_{max}$, which are critical for achieving high-performance RF GFETs. By leveraging the power of AI, we can more efficiently uncover hidden relationships between gate shapes and pseudo-optic trajectories of ballistic carriers than would be possible with human intuition alone.

## ■ METHODOLOGY

**Modeling and Simulations.** Figure 1a depicts the design concepts of a DNN-supported pseudo-optic GFET. To obtain the transmission of electrons under an arbitrary gate, two key steps are taken, as schematically summarized in Figures 1b and 1c. First, the Finite-Difference Time-Domain (FDTD) method is used to simulate the electron transmission under the gate (Figure 1b). Second, the DNN is trained on the transport characteristics obtained from FDTD simulations to identify the correlation between various gate shapes and their carrier transmission (Figure 1c). Once the DNN is trained, it can be used to design a targeted transmission characteristic. In the following, we provide further elaboration on each step.

**Modeling of Pseudo-Optic Behavior of Dirac Fermions.** Graphene is characterized by the massless Dirac equation near the K points,[20] which is expressed as

$$(-i\hbar v_F \boldsymbol{\sigma} \cdot \nabla + V)\Psi = i\hbar \frac{\partial \Psi}{\partial t} \tag{1}$$

where $\Psi = (\psi_1, \psi_2)$ is the two-component pseudospinor, and $\boldsymbol{\sigma} = (\sigma_x, \sigma_y)$ denotes the Pauli matrices. The Fermi velocity is represented by $v_F$ ($\sim 10^6$ m·s$^{-1}$), whereas $V$ represents the potential barrier height encountered by electrons during ballistic motion, commonly referred to as the 'external electric potential'.[21] FDTD for massless Dirac Fermions is an ideal method for training the DNN,[21,22] as it enables the analysis of the pseudo-optics properties of arbitrary-shaped gates. For simpler gate geometries like rectangles or trapezoids, analytic or ray-tracing approaches can be used.[9] However, when training the DNN, physical phenomena such as Klein tunneling and negative refraction at p−n junctions for any shapes must be translated into a parameter space that can be used as inputs for the DNN. In the discretized massless Dirac equations, the temporal derivative of one pseudospinor $\psi_1$ is the function of the spatial derivative of the other pseudospinor $\psi_2$ (see Figure 1b). The FDTD scheme updates the pseudospinors at each time step using the spatial derivative of the other pseudospinor and the external potential. Specifically, as the temporal step $k$ advances, $\psi_1(m,n)|_{t=k+1}$ is computed based on $\psi_1(m,n)|_{t=k}$ and the spatial derivative of $\psi_2(m,n)|_{t=k}$ (eq 2). Likewise, $\psi_2(m,n)|_{t=k+1}$ is calculated based on $\psi_2(m,n)|_{t=k}$ and the spatial derivative of $\psi_1(m,n)|_{t=k}$ (eq 4). The spatial derivative is discretized using the central difference method (eqs 3 and 5):

$$\psi_1^{t+\Delta t/2}(m, n) = \left(\frac{1 - \frac{iV\Delta t}{2\hbar}}{1 + \frac{iV\Delta t}{2\hbar}}\right)\psi_1^{t-\Delta t/2}(m, n) - \left(\frac{v_F\Delta t}{1 + \frac{iV\Delta t}{2\hbar}}\right)(\partial_x - i\partial_y)\psi_2^{t}(m, n) \tag{2}$$

$$(\partial_x - i\partial_y)\psi_2{}^t(m, n) = \frac{1}{2}\left\{ \begin{array}{l} \left(\frac{1}{\Delta x} - i\frac{1}{\Delta y}\right)\psi_2{}^t(m, n) + \left(\frac{1}{\Delta x} + i\frac{1}{\Delta y}\right)\psi_2{}^t(m, n-1) \\[2mm] + \left(-\frac{1}{\Delta x} - i\frac{1}{\Delta y}\right)\psi_2{}^t(m-1, n) + \left(-\frac{1}{\Delta x} + i\frac{1}{\Delta y}\right)\psi_2{}^t(m-1, n-1) \end{array} \right\} \tag{3}$$

$$\psi_2{}^{t+\Delta t}(m, n) = \left(\frac{1 - \frac{iV\Delta t}{2\hbar}}{1 + \frac{iV\Delta t}{2\hbar}}\right)\psi_2{}^t(m, n) - \left(\frac{v_F \Delta t}{1 + \frac{iV\Delta t}{2\hbar}}\right)(\partial_x + i\partial_y)\psi_1{}^{t+\Delta t/2}(m, n) \tag{4}$$

and

$$(\partial_x + i\partial_y)\psi_1{}^{t+\Delta t/2}(m, n) = \frac{1}{2}\left\{ \begin{array}{l} \left(\frac{1}{\Delta x} + i\frac{1}{\Delta y}\right)\psi_1{}^{t+\Delta t/2}(m+1, n+1) + \left(\frac{1}{\Delta x} - i\frac{1}{\Delta y}\right)\psi_1{}^{t+\Delta t/2}(m+1, n) \\[2mm] + \left(-\frac{1}{\Delta x} + i\frac{1}{\Delta y}\right)\psi_1{}^{t+\Delta t/2}(m, n+1) + \left(-\frac{1}{\Delta x} - i\frac{1}{\Delta y}\right)\psi_1{}^{t+\Delta t/2}(m, n) \end{array} \right\} \tag{5}$$

The spatial grid spacing is denoted by $\Delta x$ and $\Delta y$, and the time step is denoted by $\Delta t$. The grid indices is denoted by $m$ and $n$. The external electric potential $V$ was the relative Dirac energy level in the source, gate, and drain regions, and had a value of greater or equal to zero.

The Gaussian wave packet is a useful input for demonstrating Klein tunneling and negative refraction, as
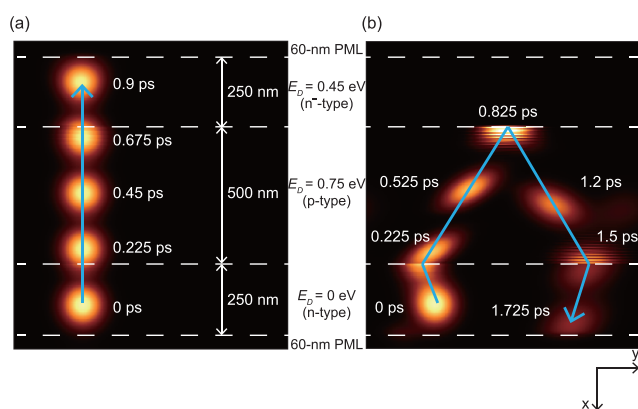


**Figure 2.** Dynamics of Gaussian electron wave packets at $n-p-n^-$ junctions. Fermi level is set to be 0.5 eV, and Dirac point level changes are marked in each region. (a) Demonstration of Klein tunneling: transmission without scattering. (b) Demonstration of negative refraction at the p−n junction (angle of incidence = 15°).

shown in Figure 2. The wave packet is generated at the source contact as[21,22]

$$\Psi(x, y; t) = N\left(\begin{array}{c} 1 \\ \frac{\hbar v_F}{E_F}(k_x + ik_y) \end{array}\right) e^{i(k_x x + k_y y - \frac{E_F}{\hbar}t)} e^{-(y-y_0)^2/\sigma_y^2 - (t-t_0)^2/\sigma_t^2} \tag{6}$$

where $N$ is the normalization constant, $E_F$ is Fermi level relative to Dirac point, $y_0$ is initial point at the source contact, $t_0$ is arbitrary time shift, and $k = (k_x, k_y)$ is the wavevector. $\sigma_y$ is related to the full-width half-maximum (FWHM) of the Gaussian wave packet ($1.6\ \sigma_y \approx$ FWHM). Considering the electrons' mean free path is several 100 nm,[23−25] $\sigma_y = 100$ nm was used. A Gaussian wave packet in spatial coordinates undergoes a Fourier transform to become a Gaussian wave packet in momentum space. Consequently, Gaussian wave packets inherently possess both position and momentum distributions. The wavenumber uncertainty is equivalent to its standard deviation, and the mean of the wavenumber determines the direction of electron propagation. In addition, to make Gaussian wave packet isotropic, $\sigma_t = 100$ fs was used. Since the energy uncertainty obtained with $\sigma_t$ is equal to 4.65 meV, electrons with a fine energy range was described in the FDTD simulation. For the FDTD simulation, a simulation domain of 1 $\mu$m × 1 $\mu$m was discretized with the 2,000 × 2,000 grids ($\Delta x = \Delta y = 0.5$ nm) and $\Delta t = \Delta x/2v_F = 0.25$ fs. Perfectly matched layers (PML) were attached to the top and bottom boundaries to prevent unwanted reflections. These PML layers were incorporated by assigning a negative value to the imaginary part of $V_{PML}$ (Im$\{V_{PML}\} \approx -0.015$ eV). The case of Klein tunneling is represented in Figure 2a, where the transmission probability ($T$) is unity regardless of the potential barrier height if the incident angle is zero.[26−28] A Gaussian excitation (bright spots), representing a ballistic Dirac Fermion, impinges perpendicular to the potential barrier and passes through without scattering. Figure 2b shows negative refractions at a p−n junction,[29,30] an essential property in graphene pseudo-optics. The negative refractions are used to suppress Klein tunneling and return a substantial portion of the excitations back to the source, creating a pinball of ballistic electrons. The electron energy dispersion in graphene is given as $E(k) = \hbar v k$ and $-\hbar v k$ for the conduction and valence bands, respectively, where $k$ and $v$ are the wavevectors and the group

velocity. $\hbar$ is the reduced Planck's constant. When an incident wave, $\boldsymbol{k}_i = (k_i\cos\theta_i, k_i\sin\theta_i)$, propagates from n-type to p-type, the wave is partially transmitted to the valence band with the wavevector $\boldsymbol{k}_t = (-k_t\cos\theta_t, -k_t\sin\theta_t)$, resulting in negative refractive index defined by Snell's law: $n = \sin\theta_i / \sin\theta_t = -k_t/k_i$. For the interfaces between the same polarities, the refractive index and the angle are positive.

**FDTD Simulations for Arbitrary-Shaped Gates.** To simulate the behavior of Dirac Fermions in the presence of an arbitrary gate structure, we discretized the gate shape into a by $100 \times 50$ grid with a spacing of 10 nm. This grid size was chosen to balance the maximum electron energy with lithographic limits, as the minimum wavelength that can be represented in FDTD is approximately ten times the grid size.[31] The FDTD grating used in the simulation was 0.5 nm, so the shortest wavelength of Dirac Fermions was 5 nm, corresponding to 0.827 eV, which is greater than 30 $k_B\Theta$ at room temperature, where $k_B$ is Boltzmann constant and $\Theta$ is temperature. Therefore, the simulation accurately represents electrons with energy $|E(\boldsymbol{k})| \leq 30\ k_B\Theta$, which is sufficient for considering the transmission and distribution function broadening.

When an arbitrary gate is positioned along the trajectory of ballistic Fermions, the resulting excitations representing Fermions undergo multiple reflections at varying angles, often giving rise to intricate and complex excitation patterns. Leveraging the capability of the FDTD method to accommodate wave superposition, our approach adeptly characterizes these dynamic systems with stability. It is important to highlight that additional influences can originate from diverse scattering mechanisms, such as lattice imperfections or inelastic scattering. Integrating these factors into the FDTD framework is technically feasible. First, the impact of uniformly distributed lattice imperfections like vacancies can be introduced as potential perturbations, denoted as $\Delta V(m, n)$, and Fermi velocity perturbations, represented as $\Delta v_F(m, n)$ in eqs 2–5. For instance, in the worst scenario where 0.01% of the carbon atoms within the gate region are lattice vacancies, this corresponds mathematically to a defect density of $3.8 \times 10^{11}$ cm$^{-2}$ (a higher density would be considered as doping), resulting in the Fermi level experience only a shift of 0.06 eV. On the contrary, in the case of nonuniformly distributed lattice vacancies, size becomes important. However, it is noteworthy that the scale of lattice vacancies is exceptionally small, measured in angstroms, even in comparison to the shortest wavelength, 5 nm, that FDTD can represent. Consequently, under the assumption of homogeneous graphene defects, the influence of lattice imperfections is included as a doping effect in our calculations, with electron dynamics anticipated to be predominantly governed by the gate field. Turning to inelastic scattering, such as electron–phonon and electron–electron scatterings, we operate within the framework of a ballistic transport regime. Subsequently, the electrons' mean free path is several 100 nm,[23−25] and we presume an average gate length similar to this value to guarantee that electron trajectories encounter minimal inelastic scattering.

To demonstrate the validity and feasibility of our scheme, we calculated the resistance of sawtooth-shaped gates, as depicted in Figure 3a, and compared them with experimental data from the literature.[32−35] These gate types have been extensively examined through both simulation[10,36−38] and experimentation.[32−35] The calculated results align with the documented resistance characteristics. As illustrated in Figure 3b, sawtooth
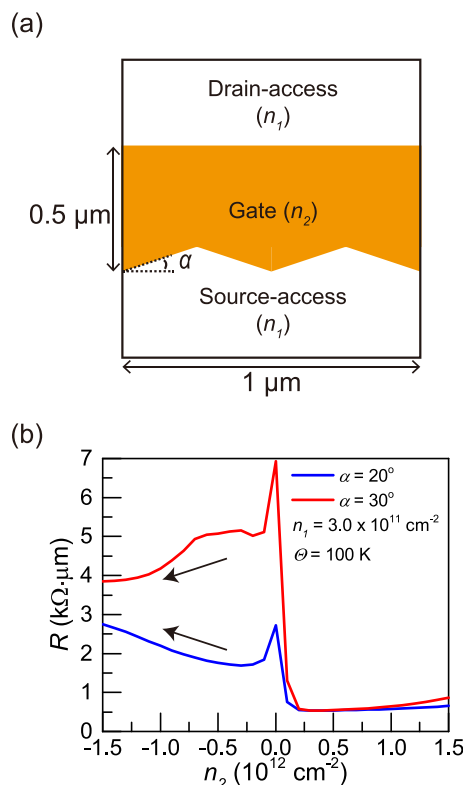
(a)



(b)



**Figure 3.** (a) Configuration of the sawtooth-shaped gate. In this figure, "$n$" denotes the carrier density, with negative values indicating p-type carriers. (b) Resistance characteristics as a function of the carrier density in the gate region for abrupt junctions. The resistance, $R$, is defined as the inverse of the conductance $G$. In equilibrium, conductance $G$ is derived from eq 7, calculated as $(2q^2/h)[\int T(E) M(E)(-\partial f/\partial E)dE]$.

angles ($\alpha$) of 20° and 30° exhibit resistance peaks when the carrier type in the gate region is intrinsic. At an angle of 20°, an increase in resistance is observed as the gate assumes more p-type characteristics, indicating a decrease in off-state current. Conversely, at an angle of 30°, the resistance trend mirrors that observed in typical graphene FETs, without the enhancement seen at 20°. Although a one-to-one match in absolute numbers between simulation and experiment is unrealistic due to external factors such as contact resistance, which varies significantly with individual fabrication processes, the key physical features are all successfully predicted by our scheme. This indicates that the gate shape remains a critical parameter influencing these properties, even though assumptions of ballistic transport and minimal inelastic scattering may complicate the precise prediction of the electrical properties of graphene devices with nonrectangular gates. Consequently, our FDTD approach provides a practical method for predicting the electrical properties of graphene devices. Furthermore, the potential application of DNN-based gate design is promising and will be elaborated upon in future sections.

To ensure numerical stability of FDTD, we set the temporal step ($\Delta t$) to $\Delta x/2v_F = 0.25$ fs, where $v_F$, the Fermi velocity, was set to $10^6$ m·s$^{-1}$. Additionally, since the resolution of electron beam lithography is less than 10 nm × 10 nm, defining this grid size lithographically poses no issue, making the examined gate structures practically feasible. The FDTD simulation of the GFET structure, as shown in Figure 1c, was performed considering the effects of the applied drain-source
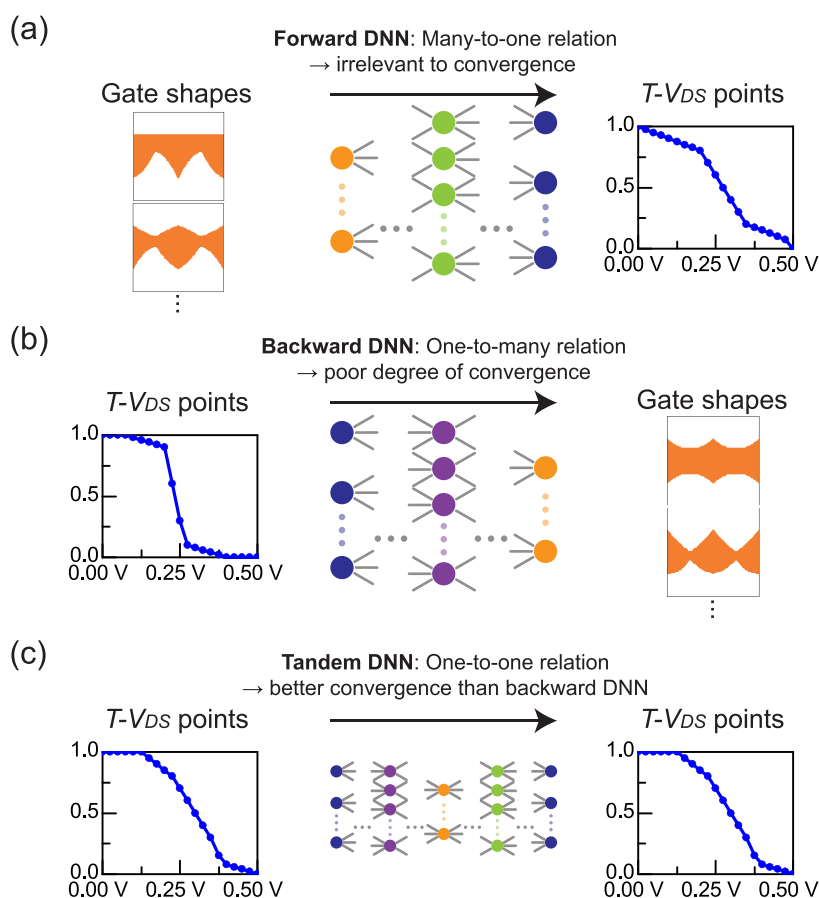
**Figure 4.** Structures of forward, backward, and tandem DNNs. (a) Forward DNN: the many-to-one relation is not relevant to convergence because the forward DNN is trained to ensure that the $T-V_{DS}$ characteristic of the gate shape matches the FDTD simulation results. (b) Backward DNN: one-to-many relation adversely affects the degrees of convergence when training DNN. (c) Tandem DNN: one-to-one relation has much lower loss than one-to-many relation. The backward DNN was constructed with 20 units (input layer: $T-V_{DS}$ points) - 100 neurons - ReLU activation - 50 - ReLU - 50 - ReLU - 6 - [50 × Sigmoid activation] - 6 units (output layer: gate shape parameters (Figure 7a)). The forward DNN was constructed of 6 units (input layer: gate shape parameters) - 50 neurons - ReLU activation - 50 - ReLU - 50 - ReLU - 50 - ReLU - 20 - Sigmoid activation - 20 units (output layer: $T-V_{DS}$ points).

voltage ($V_{DS}$) in combination with the top and bottom gate voltages. In our analysis, we considered the vertical electric field resulting from the gate biases to have a greater impact on the graphene channel compared to the horizontal electric field generated by the drain-source bias. Thus, the simulation was conducted under a weak-bias condition for $V_{DS}$. Then, we assumed a 1.6 nm $SiO_2$ gate insulator between the arbitrary gate and the graphene channel and a 90 nm $SiO_2$ back gate insulator. The top and bottom gates were biased at 0.1 and 50 V, respectively, while the Fermi levels under the gate region were defined as the average of the source and the drain sides to operate in the ballistic regime.[39] The calculation of the channel potential, which accounts for the disparity between the Dirac and Fermi energy levels, was performed by incorporating the quantum capacitance characteristics of the graphene channel in the FET structure (Figure 1c) into Poisson's equation.[40−42] This yielded the potential for each region, which was then used to determine the external electric potential $V$. To calculate the transmission probability-drain voltage ($T$-$V_{DS}$) curves for an arbitrary gate shape when electron's energy was matched to electrochemical potential of drain, we performed FDTD simulations for 20 points of $V_{DS}$ from 0.0 to 0.5 V with a 0.025 V step.

To simulate RF FETs using FDTD, a periodic boundary condition was applied to the left and right edges of the simulation domain (the $y$-direction in Figure 2) to account for the wider widths of RF FETs (typically greater than 1 $\mu$m). This allowed for the representation of wider gates where the unit cell is repeated. An arbitrary gate shape was placed in the middle (the $x$-direction) of the simulation domain within a 1 $\mu$m × 0.5 $\mu$m region. Even in the worst-case scenario where the gate length is 0.5 $\mu$m due to full metal coverage, the $f_T$ can reach up to 2.54 THz, given the usual electron mobility of graphene (ranging from 80,000 to 230,000 $cm^2 \cdot V^{-1} \cdot s^{-1}$).[43,44] This is a significant improvement compared to conventional semiconductor FETs with the same gate length. Moreover, the 0.5 $\mu$m gate length is wide enough for modern lithography technology to implement sophisticated edge shapes that can potentially improve $f_{max}$ and $r_{out}$. Therefore, GFETs have the potential to become a competitive candidate for high-power RF devices due to their excellent current handling capacity.

**Gate Design by a Deep Neural Network.** To address convergence issues, we utilized a tandem deep neural network (DNN) structure constructed using TensorFlow,[45] a library for large-scale machine learning. The DNNs were trained on a data set obtained from FDTD simulations of arbitrary gate shapes. Although the trained DNN can be used for direct

design, the inverse scattering problem poses a challenge in DNN-supported design. While a forward DNN (Figure 4a) can be trained to estimate the $T$-$V_{DS}$ of an arbitrary gate shape, a backward DNN (Figure 4b) can suffer from poor convergence if multiple gate shapes correspond to one $T$-$V_{DS}$ input (one-to-many relation). Design results using only the backward DNN are therefore unsatisfactory. To overcome this challenge, various approaches such as tandem DNN and bidirectional network have been proposed.[15,46] In our study, we adopted a tandem DNN structure (Figure 4c) that combines an extra backward DNN with the forward DNN. The forward DNN is first trained with a large data set and its weights are fixed. Then, the backward DNN is connected to the front end of the forward DNN and trained to ensure that each gate has a unique $T$-$V_{DS}$ curve defined by the preconditioned forward DNN. This approach ensures consistent convergence of the tandem DNN.

The training data set used for DNN-supported designs plays a critical role in determining their effectiveness. In our study, the gate shapes were arbitrary within a $50 \times 50$ grid but not entirely random. They had six arbitrary structural parameters, namely two lengths ($L_1$, $L_2$) and four sine wave magnitudes ($C_1 \sim C_4$) (Figures 4 and 7a). GFETs with gate shape that had just one length parameter (or angle parameter), such as trapezoid or sawtooth,[9,10] have shown increased RF or logic performance. Building upon these shapes, in order to expand the degree of freedom, additional length parameter and curvature parameters were introduced. To be more specific, for instance, the line by

$$x = -\frac{L_1 - L_{SA}}{W/4}y - C_1 \sin\left(\frac{\pi}{W/4}y\right) + L_{ch} - L_{SA}$$

defines the boundary that is determined by $L_1$ and $C_1$ when $0 \le y \le W/4$. All parameters are in nanometers, and $C_1$ can be negative. In addition, the width ($W$) is 1000 nm, while the length of channel ($L_{ch}$) and source-access region ($L_{SA}$) are 1000 and 250 nm, respectively. This guided structure explains why DNN-supported design can be likened to a pinball game with roughly predetermined paths. Using completely random gate shapes would be impractical due to the vast number of possible gate shapes. There are $50 \times 50$ grids, and each grid has two states for the gate metal coverage—filled or empty. The resulting cases are $2^{2,500}$ (roughly $10^{750}$), making it challenging to obtain satisfactory results without enormous computing resources and data sets. Moreover, a completely random approach (Figure 5a) can result in designed gate shapes that consist of isolated metal islands, which would require the synchronous control of multiple nanoscale electrodes, making
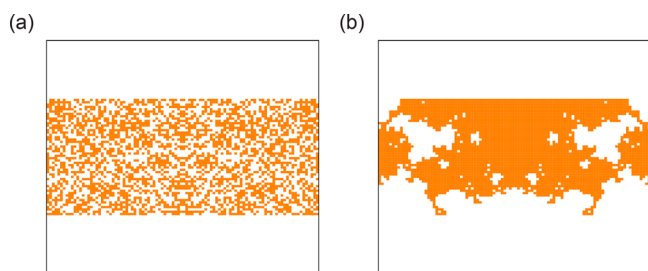
it unfeasible. To address this issue, we tried a two-dimensional random walk algorithm (Figure 5b) to form electrically connected gate shapes as input data sets. As shown in Figure 5b, the presence of holes in the gate shape, as well as the complex interface shape between the gate region and the source-access (or drain-access) region, can potentially enhance the suppression of electron transmission more effectively than relying solely on multiple structural parameters. However, it is important to note that this approach also presents limitations, as the resulting inverse design may not guarantee a connected configuration similar to that depicted in Figure 5a. Therefore, guidelines for the ballistic electrons' paths were necessary, which were realized by the structural parameters of length, curvature, and angles.

The forward DNN consisted of four hidden layers, each containing 50 neurons, while the backward DNN had three hidden layers with 100, 50, and 50 neurons, respectively. Rectified linear activation functions (ReLUs) were used in the output of each layer, except for the last one, which had a sigmoid activation function. Although applying an activation function to the output layer is uncommon in regression problems, it was beneficial for our gate design since the gate shape is defined within the rectangle of $L_{g,max} \times W$, and the transmission probability is also within the range from zero to unity. This made the DNN losses lower when an activation function was applied to the output layer. Table 1 summarizes

**Table 1. Hyper-Parameters and Losses of DNNs**

| Hyper-parameters | Forward DNN | Backward DNN |
|---|---|---|
| Data set size | 12800 | 12800 |
| Training set size | 8960 | 8960 |
| Test set size | 3840 | 3840 |
| Optimizer | Adam | Adam |
| Learning rate | 0.001 | 0.001 |
| Batch size | 256 | 256 |
| Batch normalization | YES | YES |
| Epochs | 10000 | 10000 |
| Activation function | ReLU, Sigmoid | ReLU, Sigmoid |
| Train MSE | 0.000252 | 0.000471 (Tandem DNN) |
| Test MSE | 0.000384 | 0.000501 (Tandem DNN) |

the training-related parameters. Mean squared errors (MSEs) were used to evaluate the DNNs. After 10,000 epochs, the forward DNN achieved a test MSE of 0.000384, which is comparable to the MSE of a well-trained DNN in nano-photonics (0.00035).[18] Moreover, after 10,000 epochs, the tandem DNN achieved a test MSE of 0.000501, which is similar to the test MSE of the forward DNN.

The tandem DNN, which consisted of the forward and backward DNNs, was trained to design an optimized gate shape to achieve the desired $T$-$V_{DS}$ curve. To verify the accuracy of the inverse design result, the $T$-$V_{DS}$ curves of the DNN-designed gate were recalculated using the forward DNN, and the results were compared to those obtained from the FDTD simulation, as shown in Figure 6. The curves were found to be almost identical, except for a slight difference between $V_{DS}$ values of 0.4 and 0.5 V, which was due to the errors from the forward DNN. Nonetheless, the comparison exhibited excellent agreement overall, confirming the effectiveness of the tandem DNNs in inverse design. This was further supported by the low MSE of the tandem DNNs, as shown in Figure 6b.
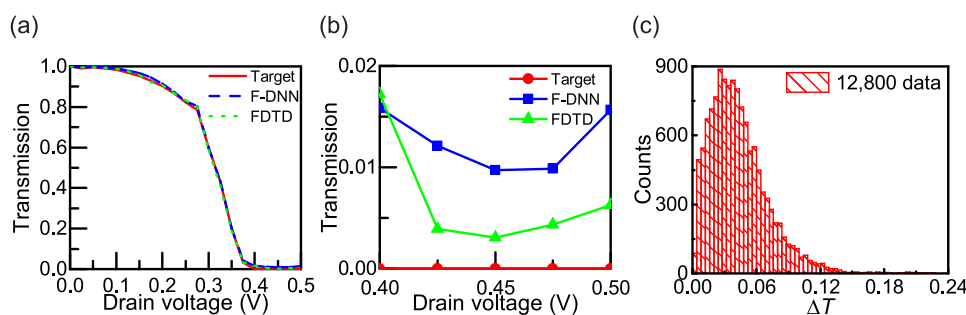


**Figure 5.** Examples of random gate shapes generated by a (a) completely random approach and (b) two-dimensional random walk algorithm.

**Figure 6.** Transmission probability results of inverse design. (a) $T-V_{DS}$ curves for the entire drain voltage range. (b) Enlarged $T-V_{DS}$ curve between $V_{DS} = 0.4$ and $0.5$ V. Target: a targeted transmission probability for drain current saturation. F-DNN: Output of the trained forward DNN when the input was the DNN-designed gate shape (Figure 7a). FDTD: FDTD simulation result with the DNN-designed gate shape. (c) Histogram of the data set as a function of $\Delta T$.

Figure 6c presents a histogram depicting the transmission deviation ($\Delta T$) of the training data set used in this study. The $\Delta T$ value was calculated as

$$\Delta T = \sum_{u=0}^{3} |T(V_{DS} = 0.4 + 0.025 \times u)$$
$$- T(V_{DS} = 0.4 + 0.025 \times (u + 1))|/4$$

This histogram illustrates the level of transmission achieved by the DNN-designed gate shape, as well as the characteristics of the training data set. A lower $\Delta T$ value indicates a higher degree of current saturation within the range of $0.4$ V $\leq V_{DS} \leq 0.5$ V. In total, the 12,800 data points were classified into 60 divisions based on $\Delta T$ values ranging from 0 to 0.24, with a step size of $\delta(\Delta T) = 0.004$. Remarkably, the DNN-designed gate shape exhibited a $\Delta T$ value of 0.003, falling within the first range ($0 \leq \Delta T < 0.004$), which contained only 87 out of the 12,800 data points. This indicates that the DNN-designed gate shape possesses an exceptional transmission suppression ability, ranking in the top 0.68% among all the data points.

## ■ RESULTS AND DISCUSSION

**DNN Designed GFET Performance.** The transmission probabilities, $T(E)$, for an arbitrary gate were obtained from response of Gaussian impulse ($\delta$-function) in the FDTD simulation. However, calculating the $T(E)$ for all incident angles with $\delta(x, y, t)$ would require multiple FDTD simulations. Therefore, adopting line excitations (i.e., $\delta(x, t)$) as the inputs can help avoid this issue. The line excitation's intensity has a Gaussian form over time and is uniform along the $y$-axis. This approach is valid as long as the particles are noninteracting, which is the case in the graphene model (massless Dirac Fermion). It also helps to reduce numerical noise from the discretization of $\theta_S$. Note that the $T(E)$ of a specific gate shape is also a function of the gate bias, as diffraction angles at the interfaces are dependent on the source-to-gate and the gate-to-drain Dirac level differences. To obtain the DNN training and design data, the responses at $V_{g\,top} = 0.1$ V were used.

The DNN was trained to optimize the gate shape in order to achieve a targeted $T$-$V_{DS}$ curve by maximizing reflections and minimizing transmissions. The typical transmission paths in a rectangular gate of the traditional GFET involve refraction, reflection, and Klein tunneling. To minimize these paths, the optimized gate edges—the source and drain sides—are not simple straight lines (as shown in Figure 7a). The curvatures and slopes on both sides suppress electron transmission more
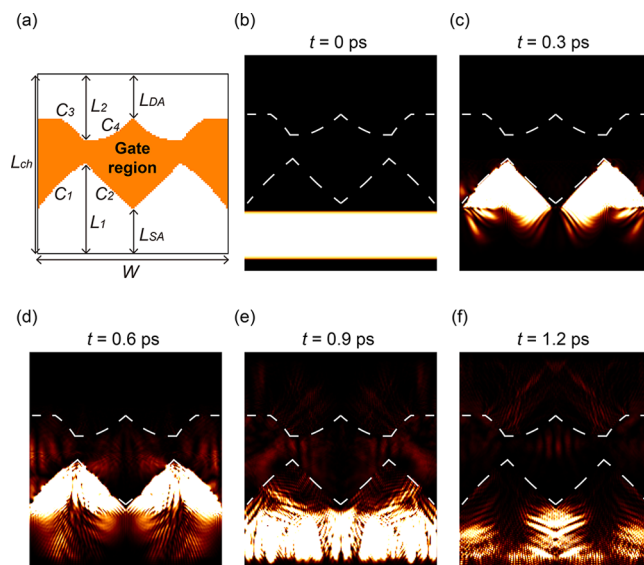


**Figure 7.** DNN-designed gate shape and dynamics of the line electron wave packet of GFET. (a) DNN-designed gate shape according to the targeted $T-V_{DS}$ curve. The gate shape had six structural parameters: two lengths ($L_1$, $L_2$) and four sine wave magnitudes ($C_1 \sim C_4$). Channel length $L_{ch} = 1$ $\mu$m, channel width $W = 1$ $\mu$m, source-access region length $L_{SA} = 250$ nm, and drain-access region length $L_{DA} = 250$ nm. The maximum value of the gate length was limited as $L_{g,max} = L_{ch} - L_{SA} - L_{DA} = 500$ nm. The DNN-designed gate shape has the parameters as $L_1 = 500$ nm, $L_2 = 370$ nm, $C_1 = 22$ nm, $C_2 = -12$ nm, $C_3 = 58$ nm, and $C_4 = -34$ nm. Positive and negative values in sine wave magnitude $C$ indicate bends toward the drain and source, respectively. (b–f) Dynamics of the line electron wave packet of GFET with the DNN-designed gate shape in FDTD simulation.

effectively than variations on one edge, such as a trapezoidal gate. A detailed analysis of the optimized gate using FDTD simulation (Figures 7b-f) revealed that the DNN designs a gate in which most of the electrons are screened by the first edge— the source side curvature. However, some sharp tips exist at the junction of the two curves, and these act as leak points. The sharp tips behave like a point source of spherical wavelets in the Huygens-Fresnel principle. To suppress these residual transmissions, the DNN uses the second screen—the drain side curvature. Consequently, some electrons are hovering under the gate due to multiple reflections at the two edges. However, only a small fraction of electrons reaches the drain electrode, indicating that the DNN-designed gate successfully creates a transport gap. It is captivating to observe the resonating

excitations between the two edges, which give rise to intricate chaotic patterns upon reflection from the edge surfaces, as illustrated in Figures 7d-f. These distinctive pseudo-optical characteristics can be classified as manifestations of chaotic dynamics within graphene cavities. Notably, the exploration of chaotic dynamics has also extended to the realm of bilayer graphene in recent studies.[47]

Figures 8a-c illustrate the effects of individual design parameters on electron transmission suppression in graphene
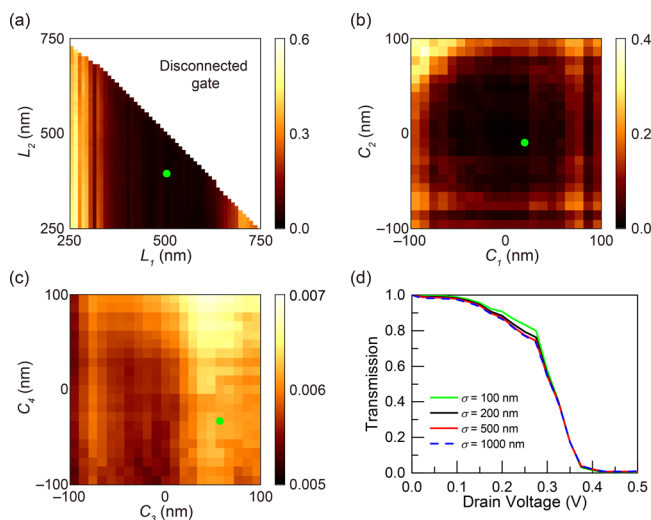


**Figure 8.** Transmission probabilities as a function of varying design parameters when the electron's energy was matched to the electrochemical potential of the drain voltage (0.5 V): (a) length $L_1$ and $L_2$, (b) sine wave magnitudes $C_1$ and $C_2$, and (c) sine wave magnitudes $C_3$ and $C_4$. For each subplot, the design parameters not explicitly varied were held constant at the values determined by the DNN, as detailed in Figure 7. Additionally, the DNN-optimized parameter sets are highlighted with green points. (d) Transmission probabilities as a function of the FDTD simulation parameter, $\sigma$ ($\sigma_y$ as defined in eq 6), which is pertinent to the electrons' mean free path.

FETs. Notably, parameters associated with the source side, where electrons first interact, exhibit a significant impact on transmission suppression. Specifically, alterations in the parameter $L_1$ are observed to markedly influence electron transmission probability, demonstrating greater sensitivity compared to changes in $L_2$. Moreover, inappropriate selections of sine wave magnitudes $C_1$ and $C_2$ can lead to an increase in transmission probability by up to 0.4. Conversely, $C_3$ and $C_4$ contribute primarily to the fine-tuning of transmission probabilities, a phenomenon further elaborated upon in Figure 7. Additionally, an increased mean free path, which is associated with high mobility, results in a reduced electron transmission probability in devices with identical gate configurations, as depicted in Figure 8d. This observation underscores the critical role of mean free path in the electrical characteristics of devices and in the optimization of gate shapes.

The Landauer formula[48] was used to calculate the current–voltage ($I_{DS}$-$V_{DS}$) relations after obtaining the transmission probability, $T$, for each bias condition:

$$I_{DS} = \frac{2q}{h} \int T(E)M(E)[f(\mu_S) - f(\mu_D)]dE \quad (7)$$

where $M$ is the number of modes, $q$ is the charge of the electron, $h$ is Planck's constant, and $f$ is the Fermi–Dirac

distribution. $\mu_S$ and $\mu_D$ are electrochemical potentials of the source and drain, respectively. The number of modes $M$ is approximated as $M(E) \approx W|E|/\pi\hbar v_F$.[35] The current–voltage characteristics of the DNN-deigned GFET (DNN-GFET) and a conventional GFET (c-GFET) were calculated for three different gate voltages ($V_{g\,bot}$ = 50, 75, and 100 V) using the Landauer formula. The response of c-GFET was obtained using a conventional rectangular gate with the same effective gate length. The resulting $I_{DS}$-$V_{DS}$ curves are compared in Figure 9. The DNN-GFET showed distinct drain current
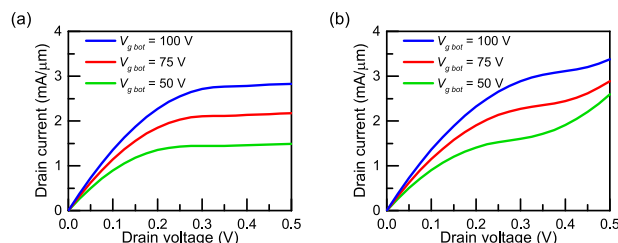


**Figure 9.** $I_{DS}$–$V_{DS}$ characteristics for DNN-designed GFET and conventional GFET. (a) DNN-designed GFET. (b) Conventional GFET.

saturation, which was lacking in the c-GFET, demonstrating the effectiveness and usefulness of the proposed approach. Even though the responses at a single bias point ($V_{g\,bot}$ = 50 V) were used to train the DNN, the DNN-GFET reproduced $I_{DS}$ saturations under other gate bias conditions. The potential drop across the graphene channel ($|E_{F,\,ch}|$) is slightly changed despite huge change of bottom gate bias, being 0.25, 0.31, and 0.36 eV for the gate bias $V_{g\,bot}$ = 50, 75, and 100 V, respectively. The quantum capacitance effect was included in the calculations.[40−42] While the gate voltage changes by 25 V (from $V_{g\,bot}$ = 50 to 75 V), the potential drop across the graphene channel changes only by 0.06 eV, indicating minimal variation of energy band across the channel and little influence on the electron scattering from the band bending. However, the DNN-GFET exhibited significant current saturations induced by the gate shape, specifically, the lateral distribution of the energy barrier by inducing the negative refractions. Therefore, the inherent pseudo-optic nature of graphene was more effective than the variations in the energy barrier height based on the source-drain potential difference.

We report on the substantially improved radiofrequency (RF) performance of deep neural network (DNN)-guided graphene field-effect transistors (GFETs), highlighting key performance parameters. The transconductance ($g_m$) and output impedance ($r_{out}$) were calculated by taking derivatives of the $I_{DS}$-$V_{DS}$ characteristics, using finite voltage differences of $\Delta V_{GS} = \Delta V_{DS} = 0.025$ V as

$$g_m = \frac{\partial I_{DS}}{\partial V_{GS}} \approx \frac{I_{DS}(V_{GS} + \Delta V_{GS}) - I_{DS}(V_{GS})}{\Delta V_{GS}} \quad (8)$$

$$r_{out} = g_{ds}^{-1} = \left(\frac{\partial I_{DS}}{\partial V_{DS}}\right)^{-1} \approx \left(\frac{I_{DS}(V_{DS} + \Delta V_{DS}) - I_{DS}(V_{DS})}{\Delta V_{DS}}\right)^{-1} \quad (9)$$

At $V_{g\,top}$ = 0.1 V, $V_{g\,bot}$ = 50 V and $V_{DS}$ = 0.5 V, the DNN-GFET showed $g_m$ = 6.4 mS·$\mu$m$^{-1}$ and $r_{out}$ = 7.55 kΩ·$\mu$m, while the c-GFET had $g_m$ = 2.0 mS·$\mu$m$^{-1}$ and $r_{out}$ = 0.16 kΩ·$\mu$m. $g_m$ in DNN-GFET was about 3 times larger than that of c-GFET, and $r_{out}$ was over 45 times larger. This substantial improvement

in rout led to increased $f_T$ and $f_{max}$. We estimated $f_T$ and $f_{max}$ using the small-signal equivalent circuit,[49,50] where

$$f_T \approx \frac{g_m}{2\pi} \frac{1}{(C_{gs} + C_{p,gs} + C_{p,gd})(1 + g_{ds}(R_S + R_D)) + C_{p,gd}g_m(R_S + R_D)} \tag{10}$$

$$f_{max} \approx \frac{f_T}{2\sqrt{g_{ds}(R_G + R_S) + 2\pi f_T R_G C_{p,gd}}} \tag{11}$$

Here, $C_{gs}$ is the gate capacitance, and $C_{p,gs}$ and $C_{p,gd}$ are the parasitic gate-source and gate-drain capacitances, respectively. $R_S$ and $R_D$ are the parasitic resistances of the source and drain, and $R_G$ is the gate resistance. We used an averaged effective gate length of $L_{g,eff}$ = 312.4 nm for DNN-GFETs with nonuniform gate length. The parasitic capacitances and resistances were collected from experimental results of a c-GFET with $L_g \sim$ 300 nm,[51−53] which is similar to that of the DNN-GFET. Specifically, $C_{gs}$ = 8.0 fF·$\mu m^{-1}$, $C_{p,gs}$ = 0.8 fF·$\mu m^{-1}$, $C_{p,gd}$ = 0.8 fF·$\mu m^{-1}$, $R_{S,D}$ = 100 $\Omega$·$\mu m$, and $R_G$ = 1 k$\Omega$·$\mu m$. For c-GFETs of this size, $f_T$ typically ranged from 10 to 50 GHz. Our theoretical estimation for the c-GFET with $L_{g,eff}$ was $f_T$ = 14.5 GHz, which is consistent with experimental observations. However, $f_{max}$ was only 2.8 GHz for the c-GFET, whereas the DNN-GFET showed $f_T$ = 93.6 GHz and $f_{max}$ = 59.6 GHz. These improvements in $f_T$ and $f_{max}$ were achieved without compromising the mobility, by utilizing the inherent properties of graphene. Moreover, if DNN-GFETs are combined with recent advances in fabrication, they can operate at even higher frequencies. Previous attempts to improve $f_{max}$ of c-GFETs involved using a multifinger embedded T-gate or reducing the parasitic components.[54,55] If the DNN-GFET adopts such a T-gate with $R_G$ = 10 $\Omega$·$\mu m$, $f_{max}$ can reach up to 337 GHz with the same gate shape.

Compared to our previous work,[56] we found that the transmission probability, which ranges between zero and one, is a more effective training parameter than the unbounded and unreferenced drain current. In our earlier study, a DNN trained with drain current resulted in a GFET with a $f_{max}$ of only 18 GHz for a $L_{g,eff}$ of 363.4 nm. Because the drain current is unbounded, the DNN output required multiple sigmoid functions, and the degree of convergence depended on the number of sigmoid functions used. However, when we used the transmission probability as the input data set, the DNN output could be used as-is, leading to a substantial improvement in RF characteristics. Therefore, projecting the infinite space onto a manageable finite space provides a more efficient DNN-supported design that reduces the degrees of freedom.

Our method of constraining the gate shape using just six parameters is a form of projection. Despite seemingly limited degrees of freedom, with only 50 grids per axis, the possibilities can expand to a virtually infinite number, around $10^{750}$. Our approach determines the paths of ballistic electrons, similar to the paths in a pinball game, even though the number of parameters is reduced. These parameters are still beyond human intuition, but the DNNs we trained can efficiently achieve the desired design goals. We discovered that holes, or ungated isolated regions in the gate, were efficient in holding electrons back. Electrons tend to hover around these holes due to multiple reflections at the edges, similar to echoes. Additionally, our method can be extended to train a DNN to design the gates' vertical structures in addition to the graphene pseudo-optics lateral structure. Parasitic components such as resistance and capacitance affect $f_T$ and $f_{max}$, and the

gate's cross-sectional shape has the most significant impact on these parameters. A DNN can design a gate shape applicable to a real RF device if it learns the correlations between the gate shape and extrinsic components as well as the transmission probability by graphene pseudo-optics.

## ■ CONCLUSIONS

In summary, we have demonstrated the effectiveness of using DNNs to design high-performance graphene RF FETs by incorporating graphene pseudo-optics and machine learning. Our approach successfully generated a transport gap while maintaining the electron mobility, resulting in a significant improvement in RF performance and drain current saturation. Our method is not limited to RF GFET design and can be extended to various design goals, including logic devices and nonlinear devices. By training the DNN to optimize the on/off ratio, our approach can also be used to design improved switching GFETs. Overall, this work provides a promising path for the efficient design and optimization of graphene-based devices through the integration of machine learning and the unique properties of graphene.

## ■ AUTHOR INFORMATION

### Corresponding Author

**Byoung Don Kong** − *Department of Electrical Engineering, Pohang University of Science and Technology (POSTECH), Pohang 37673, Republic of Korea;* ⊙ orcid.org/0000-0003-4072-4399; Email: bdkong@postech.ac.kr

### Authors

**Gyeong Min Seo** − *Department of Electrical Engineering, Pohang University of Science and Technology (POSTECH), Pohang 37673, Republic of Korea*

**Chang-Ki Baek** − *Department of Electrical Engineering and Department of Convergence IT Engineering, Pohang University of Science and Technology (POSTECH), Pohang 37673, Republic of Korea;* ⊙ orcid.org/0000-0002-2852-6683

Complete contact information is available at:
https://pubs.acs.org/10.1021/acsaelm.4c00236

### Notes

The authors declare no competing financial interest.

## ■ ACKNOWLEDGMENTS

## ■ REFERENCES

(1) Champlain, J. G. A first principles theoretical examination of graphene-based field effect transistors. *J. Appl. Phys.* **2011**, *109* (8), No. 084515.

(2) Han, M. Y.; Özyilmaz, B.; Zhang, Y.; Kim, P. Energy band-gap engineering of graphene nanoribbons. *Physical review letters* **2007**, *98* (20), 206805.

(3) Chen, Z.; Lin, Y.-M.; Rooks, M. J.; Avouris, P. Graphene nano-ribbon electronics. *Physica E: Low-dimensional Systems and Nanostructures* **2007**, *40* (2), 228−232.

(4) Yinxiao Yang; Murali, R. Impact of size effect on graphene nanoribbon transport. *IEEE Electron Device Lett.* **2010**, *31* (3), 237−239.

(5) Ni, Z. H.; Yu, T.; Lu, Y. H.; Wang, Y. Y.; Feng, Y. P.; Shen, Z. X. Uniaxial strain on graphene: Raman spectroscopy study and band-gap opening. *ACS Nano* **2008**, *2* (11), 2301−2305.

(6) Pereira, V. M.; Castro Neto, A. H.; Peres, N. M. R. Tight-binding approach to uniaxial strain in graphene. *Phys. Rev. B* **2009**, *80* (4), No. 045401.

(7) Choi, S.-M.; Jhi, S.-H.; Son, Y.-W. Effects of strain on electronic properties of graphene. *Phys. Rev. B* **2010**, *81* (8), No. 081407.

(8) Cocco, G.; Cadelano, E.; Colombo, L. Gap opening in graphene by shear strain. *Phys. Rev. B* **2010**, *81* (24), 241412.

(9) Tan, Y.; Elahi, M. M.; Tsao, H.-Y.; Habib, K. M.; Barker, N. S.; Ghosh, A. W. Graphene Klein tunnel transistors for high speed analog RF applications. *Sci. Rep.* **2017**, *7* (1), 9714.

(10) Jang, M. S.; Kim, H.; Son, Y.-W.; Atwater, H. A.; Goddard, W. A., III Graphene field effect transistor without an energy gap. *Proc. Natl. Acad. Sci. U. S. A.* **2013**, *110* (22), 8786−8789.

(11) Ji, S.; Xu, W.; Yang, M.; Yu, K. 3D convolutional neural networks for human action recognition. *IEEE transactions on pattern analysis and machine intelligence* **2013**, *35* (1), 221−231.

(12) Hinton, G.; Deng, L.; Yu, D.; Dahl, G.; Mohamed, A.-r.; Jaitly, N.; Senior, A.; Vanhoucke, V.; Nguyen, P.; Sainath, T.; Kingsbury, B. Deep neural networks for acoustic modeling in speech recognition: The shared views of four research groups. *IEEE Signal processing magazine* **2012**, *29* (6), 82−97.

(13) Carleo, G.; Cirac, I.; Cranmer, K.; Daudet, L.; Schuld, M.; Tishby, N.; Vogt-Maranto, L.; Zdeborová, L. Machine learning and the physical sciences. *Rev. Mod. Phys.* **2019**, *91* (4), No. 045002.

(14) Carleo, G.; Troyer, M. Solving the quantum many-body problem with artificial neural networks. *Science* **2017**, *355* (6325), 602−606.

(15) Liu, D.; Tan, Y.; Khoram, E.; Yu, Z. Training deep neural networks for the inverse design of nanophotonic structures. *Acs Photonics* **2018**, *5* (4), 1365−1369.

(16) Peurifoy, J.; Shen, Y.; Jing, L.; Yang, Y.; Cano-Renteria, F.; DeLacy, B. G.; Joannopoulos, J. D.; Tegmark, M.; Soljačić, M. Nanophotonic particle simulation and inverse design using artificial neural networks. *Science advances* **2018**, *4* (6), eaar4206.

(17) Ma, W.; Cheng, F.; Liu, Y. Deep-learning-enabled on-demand design of chiral metamaterials. *ACS Nano* **2018**, *12* (6), 6326−6334.

(18) An, S.; Fowler, C.; Zheng, B.; Shalaginov, M. Y.; Tang, H.; Li, H.; Zhou, L.; Ding, J.; Agarwal, A. M.; Rivero-Baleine, C.; et al. A deep learning approach for objective-driven all-dielectric metasurface design. *ACS Photonics* **2019**, *6* (12), 3196−3207.

(19) Wan, J.; Jiang, J.-W.; Park, H. S. Machine learning-based design of porous graphene with low thermal conductivity. *Carbon* **2020**, *157*, 262−269.

(20) Castro Neto, A. H.; Guinea, F.; Peres, N. M. R.; Novoselov, K. S.; Geim, A. K. The electronic properties of graphene. *Rev. Mod. Phys.* **2009**, *81* (1), 109.

(21) Jang, M. S.; Kim, H.; Atwater, H. A.; Goddard, W. A. Time dependent behavior of a localized electron at a heterojunction boundary of graphene. *Appl. Phys. Lett.* **2010**, *97* (4), No. 043504.

(22) Fernandes, D. E.; Rodrigues, M.; Falcao, G.; Silveirinha, M. G. Time evolution of electron waves in graphene superlattices. *AIP Advances* **2016**, *6* (7), No. 075109.

(23) Tse, W.-K.; Hwang, E.; Das Sarma, S. Ballistic hot electron transport in graphene. *Appl. Phys. Lett.* **2008**, *93* (2), No. 023128.

(24) Du, X.; Skachko, I.; Barker, A.; Andrei, E. Y. Approaching ballistic transport in suspended graphene. *Nature Nanotechnol.* **2008**, *3* (8), 491−495.

(25) Li, Q.; Das Sarma, S. Finite temperature inelastic mean free path and quasiparticle lifetime in graphene. *Phys. Rev. B* **2013**, *87* (8), No. 085406.

(26) Klein, O. Die Reflexion von Elektronen an einem Potentialsprung nach der relativistischen Dynamik von Dirac. *Zeitschrift für Physik* **1929**, *53* (3−4), 157−165.

(27) Katsnelson, M. I.; Novoselov, K. S.; Geim, A. K. Chiral tunnelling and the Klein paradox in graphene. *Nat. Phys.* **2006**, *2* (9), 620−625.

(28) Allain, P. E.; Fuchs, J.-N. Klein tunneling in graphene: optics with massless electrons. *European Physical Journal B* **2011**, *83*, 301−317.

(29) Cheianov, V. V.; Fal'ko, V.; Altshuler, B. The focusing of electron flow and a Veselago lens in graphene pn junctions. *Science* **2007**, *315* (5816), 1252−1255.

(30) Lee, G.-H.; Park, G.-H.; Lee, H.-J. Observation of negative refraction of Dirac fermions in graphene. *Nat. Phys.* **2015**, *11* (11), 925−929.

(31) Taflove, A.; Hagness, S. C. *Computational electromagnetics: the finite-difference time-domain method*; Artech House: Norwood, 2000.

(32) Sajjad, R. N.; Sutar, S.; Lee, J.; Ghosh, A. W. Manifestation of chiral tunneling at a tilted graphene p−n junction. *Phys. Rev. B* **2012**, *86* (15), 155412.

(33) Sutar, S.; Comfort, E.; Liu, J.; Taniguchi, T.; Watanabe, K.; Lee, J. Angle-dependent carrier transmission in graphene p−n junctions. *Nano Lett.* **2012**, *12* (9), 4460−4464.

(34) Morikawa, S.; Wilmart, Q.; Masubuchi, S.; Watanabe, K.; Taniguchi, T.; Plaçais, B.; Machida, T. Dirac fermion reflector by ballistic graphene sawtooth-shaped npn junctions. *Semicond. Sci. Technol.* **2017**, *32* (4), No. 045010.

(35) Wang, K.; Elahi, M. M.; Wang, L.; Habib, K. M.; Taniguchi, T.; Watanabe, K.; Hone, J.; Ghosh, A. W.; Lee, G.-H.; Kim, P. Graphene transistor based on tunable Dirac fermion optics. *Proc. Natl. Acad. Sci. U. S. A.* **2019**, *116* (14), 6575−6579.

(36) Sajjad, R. N.; Ghosh, A. W. Manipulating chiral transmission by gate geometry: switching in graphene with transmission gaps. *ACS Nano* **2013**, *7* (11), 9808−9813.

(37) Wilmart, Q.; Berrada, S.; Torrin, D.; Hung Nguyen, V; Feve, G.; Berroir, J.-M.; Dollfus, P.; Placais, B. A Klein-tunneling transistor with ballistic graphene. *2D Materials* **2014**, *1* (1), No. 011006.

(38) Elahi, M. M.; Masum Habib, K.; Wang, K.; Lee, G.-H.; Kim, P.; Ghosh, A. W. Impact of geometry and non-idealities on electron "optics" based graphene pn junction devices. *Appl. Phys. Lett.* **2019**, *114* (1), No. 013507.

(39) Datta, S. *Electronic transport in mesoscopic systems*; Cambridge university press, 1997.

(40) Fang, T.; Konar, A.; Xing, H.; Jena, D. Carrier statistics and quantum capacitance of graphene sheets and ribbons. *Appl. Phys. Lett.* **2007**, *91* (9), No. 092109.

(41) Xu, H.; Zhang, Z.; Wang, Z.; Wang, S.; Liang, X.; Peng, L.-M. Quantum capacitance limited vertical scaling of graphene field-effect transistor. *ACS Nano* **2011**, *5* (3), 2340−2347.

(42) Kong, B. D.; Jin, Z.; Kim, K. W. Hot-electron transistors for terahertz operation based on two-dimensional crystal heterostructures. *Physical Review Applied* **2014**, *2* (5), No. 054006.

(43) Yamoah, M. A.; Yang, W.; Pop, E.; Goldhaber-Gordon, D. High-velocity saturation in graphene encapsulated by hexagonal boron nitride. *ACS Nano* **2017**, *11* (10), 9914−9919.

(44) Bolotin, K. I.; Sikes, K.; Jiang, Z.; Klima, M.; Fudenberg, G.; Hone, J.; Kim, P.; Stormer, H. L. Ultrahigh electron mobility in suspended graphene. *Solid state communications* **2008**, *146* (9−10), 351−355.

(45) Abadi, M.; Agarwal, A.; Barham, P.; Brevdo, E.; Chen, Z.; Citro, C.; Corrado, G. S.; Davis, A.; Dean, J.; Devin, M. *TensorFlow: Large-scale machine learning on heterogeneous systems*; software available from tensorflow.org, 2015.

(46) Malkiel, I.; Nagler, A.; Mrejen, M.; Arieli, U.; Wolf, L.; Suchowski, H. Deep learning for design and retrieval of nano-photonic structures. *arXiv preprint arXiv:1702.07949* **2017**.

(47) Seemann, L.; Knothe, A.; Hentschel, M. Gate-tunable regular and chaotic electron dynamics in ballistic bilayer graphene cavities. *Phys. Rev. B* **2023**, *107* (20), 205404.

(48) Landauer, R. Spatial variation of currents and fields due to localized scatterers in metallic conduction. *IBM J. Res. Dev.* **1957**, *1* (3), 223−231.

(49) Rutherglen, C.; Jain, D.; Burke, P. Nanotube electronics for radiofrequency applications. *Nature Nanotechnol.* **2009**, *4* (12), 811−819.

(50) Schwierz, F. Graphene transistors. *Nature Nanotechnol.* **2010**, *5* (7), 487−496.

(51) Lin, Y.-M.; Dimitrakopoulos, C.; Jenkins, K. A.; Farmer, D. B.; Chiu, H.-Y.; Grill, A.; Avouris, P. 100-GHz transistors from wafer-scale epitaxial graphene. *Science* **2010**, *327* (5966), 662−662.

(52) Wu, Y.; Jenkins, K. A.; Valdes-Garcia, A.; Farmer, D. B.; Zhu, Y.; Bol, A. A.; Dimitrakopoulos, C.; Zhu, W.; Xia, F.; Avouris, P.; Lin, Y.-M. State-of-the-art graphene high-frequency electronics. *Nano Lett.* **2012**, *12* (6), 3062−3067.

(53) Cheng, R.; Bai, J.; Liao, L.; Zhou, H.; Chen, Y.; Liu, L.; Lin, Y.-C.; Jiang, S.; Huang, Y.; Duan, X. High-frequency self-aligned graphene transistors with transferred gate stacks. *Proc. Natl. Acad. Sci. U. S. A.* **2012**, *109* (29), 11588−11592.

(54) Han, S.-J.; Oida, S.; Jenkins, K. A.; Lu, D.; Zhu, Y. Multifinger Embedded T-Shaped Gate Graphene RF Transistors With High $f_{MAX}$/$f_T$ Ratio. *IEEE electron device letters* **2013**, *34* (10), 1340−1342.

(55) Feng, Z.; Yu, C.; Li, J.; Liu, Q.; He, Z.; Song, X.; Wang, J.; Cai, S. An ultra clean self-aligned process for high maximum oscillation frequency graphene transistors. *Carbon* **2014**, *75*, 249−254.

(56) Seo, G. M.; Baek, C.-K.; Kong, B. D. Inverse design of graphene FET by deep neural network. In *2021 IEEE 21st International Conference on Nanotechnology (NANO)*; IEEE: 2021; pp 134−137.